Spin-polarized Dirac cone, flat band and saddle point in kagome magnet YMn6Sn6
— Source link ↗

Man Li, Qi Wang, Guangwei Wang, Zhihong Yuan ...+8 more authors

Published on: 04 Dec 2020

Topics: Saddle point and Spin-½

Related papers:

- Tunable Massive Dirac Fermions in Ferromagnetic Fe 3 Sn 2 Kagome Lattice

- Evidence of orbit-selective electronic kagome lattice with planar flat-band in correlated paramagnetic YCr6Ge6

- Field-induced topological Hall effect and double-fan spin structure with a c -axis component in the metallic kagome antiferromagnetic compound Y Mn 6 Sn 6

- Dirac magnons in a honeycomb lattice quantum XY magnet CoTiO3.

- Boron Triangular Kagome Lattice with Half-Metallic Ferromagnetism

Share this paper: 📘 🐦 in ✉

Spin-polarized Dirac cone, flat band and saddle point in kagome magnet YMn6Sn6

Man Li
  Renmin University of China

Qi Wang
  Department of Physics and Beijing Key Laboratory of Opto-electronic Functional Materials & Micro-nano Devices, Renmin University of China

Guangwei Wang
  Beijing Normal University

Zhihong Yuan
  Beijing Normal University

Wenhua Song
  Renmin University of China

Rui Lou
  Lanzhou University

Zhengtai Liu
  Shanghai Institute of Microsystem and Information Technology, Chinese Academy of Sciences.

Yaobo Huang
  Shanghai Institute of Applied Physics

Zhonghao Liu
  Leibniz Institute for Solid State and Materials Research

Hechang Lei
  Renmin University of China   https://orcid.org/0000-0003-0850-8514

Zhiping Yin
  Beijing Normal University

Shancai Wang (✉ scw@ruc.edu.cn)
  Renmin University of China   https://orcid.org/0000-0001-7564-9064

Article

Spin-polarized Dirac cone, flat band and saddle point in kagome magnet YMn_6Sn_6

Man Li,[1] Qi Wang,[1] Guangwei Wang,[2] Zhihong Yuan,[2] Wenhua Song,[1] Rui Lou,[3, 4, 5] Zhengtai Liu,[6] Yaobo Huang,[7] Zhonghao Liu,[6, 8, *] Hechang Lei,[1, †] Zhiping Yin,[2, ‡] and Shancai Wang[1, §]

[1]*Department of Physics and Beijing Key Laboratory of Opto-Electronic Functional Materials&Micro-Nano Devices, Renmin University of China, Beijing 100872, China*

[2]*Department of Physics and Center for Advanced Quantum Studies, Beijing Normal University, Beijing 100875, China*

[3]*School of Physical Science and Technology, Lanzhou University, Lanzhou 730000, China*

[4]*State Key Laboratory of Surface Physics and Department of Physics, Fudan University, Shanghai 200433, China*

[5]*Collaborative Innovation Center of Advanced Microstructures, Nanjing 210093, China*

[6]*State Key Laboratory of Functional Materials for Informatics, Shanghai Institute of Microsystem and Information Technology, Chinese Academy of Sciences, Shanghai 200050, China*

[7]*Shanghai Advanced Research Institute, Chinese Academy of Sciences, Shanghai 201204, China*

[8]*College of Materials Science and Opto-Electronic Technology, University of Chinese Academy of Sciences, Beijing 100049, China*

Kagome-lattice of $3d$-transition metals hosting Weyl/Dirac fermions and topological flat bands exhibit non-trivial topological characters and novel quantum phases, such as anomalous Hall effect and fractional quantum Hall effect. With consideration of spin-orbit coupling and electron correlation, several instabilities could be induced. The complete characters of the electronic structure of kagome lattice, *i.e.* the saddle point, Dirac-cone, and flat band, around the Fermi energy (E_F) remain elusive in magnetic kagome materials. We present the first experimental observation of the complete features in ferromagnetic kagome layers of YMn_6Sn_6 helically coupled along the c-axis, by using angle-resolved photoemission spectroscopy and band structure calculations. We demonstrate a Dirac dispersion near E_F arising from a spin-polarized orbital, which carries an intrinsic Berry curvature and contributes to the anomalous Hall effect in transport measurements. In addition, a flat band and a saddle point with a high density of states and with orbital-selective characters near E_F are observed. These multi-orbital kagome features could cause multi-orbital magnetism. The Dirac fermion, flat band and saddle point in the vicinity of E_F open an opportunity in manipulating the topological properties in magnetic materials.

* lzh17@mail.sim.ac.cn

† hlei@ruc.edu.cn

‡ yinzhiping@bnu.edu.cn

§ scw@ruc.edu.cn

The frustrated kagome lattice, made up of the geometry of corner-sharing triangles, has been studied intensively due to the magnetic frustration-induced quantum spin liquid state [1, 2]. Meanwhile, the construction of topological band theory in recent years has greatly enriched in the electronic band structure of kagome lattice [3–5]. Theoretical studies show the kagome lattice systems as an ideal platform for understanding the topological states with novel topological excitations [6–8]. For example, a flat band (FB) can be constructed by completely destructive interference of Bloch wave functions in two-dimensional (2D) kagome lattice with nearest-neighbor (NN) interaction. Such FBs, just like a counterpart of the Landau level, can be characterized by a Chern number [3, 7]. Representing a highly degenerate and quenched kinetic energy of electron state may give rise to the abundant exotic emergent effects, such as ferromagnetism, high-temperature superconductivity, Wigner crystal, and fractional quantum Hall effects [9–16]. Besides, the kagome lattice system shares similar topological physics with honeycomb, Dirac cone-type dispersions in the momentum-space K point. Once a net magnetization and intrinsic spin-orbit coupling (SOC) are present, a well-separated non-trivial Chern bands, Chern gap and intrinsic quantum anomalous Hall effect could present when the Fermi energy (E_F) is tuned properly [17, 18].

The band structure studies of $3d$ transition-metal kagome compounds, which are usually strong correlated and exhibit magnetism, remain challenging albeit theoretical predictions [19–32]. A typical electronic structure of the kagome lattice is the existence of Dirac point (DP) at the Brillouin zone (BZ) corner, a saddle point (SP) at BZ boundary, and a FB over the whole BZ (Fig. 1b). Topological non-trivial electronic properties were observed in kagome lattices constituted of $3d$-transition metallic element, *i.e.*, large intrinsic anomalous Hall effect originating from the Berry curvature of Dirac cone-type dispersion of K point both in ferromagnetic (FM) and antiferromagnetic (AFM) materials [18, 20–24]. Another important feature is the dispersionless electronic structure in magnetic kagome materials [25, 30–32] and in paramagnetic (PM) kagome materials [27–29]. In PM kagome materials, extremely flat bands close to E_F have been reported in CoSn [28, 29] and YCr_6Ge_6 [27]. However, in magnetic systems, the direct evidence of the FBs is either unobserved (Fe_3Sn_2, $Co_3Sn_2S_2$ [22, 30]), or far away from E_F (FeSn [25]), due to the strong correlation of $3d$ electrons, the complexity with magnetic structure, and the interplay between electron correlation and topological properties. Thus, searching for the FBs, and saddle point, in addition to the Dirac fermions near E_F in magnetic kagome systems serves as the main objective to manipulate the topological properties in magnetic materials.

In this paper, we study the electronic structure of kagome lattice YMn_6Sn_6 with in-plane ferromagnetism and helical antiferromagnetism along c-axis by combining angle-resolved photoemission spectroscopy (ARPES) and density functional theory plus dynamical mean-field theory (DFT+DMFT) calculations. We report the first experimental observation of the complete characters of kagome electronic structure: Dirac cone, flat band and saddle point, in such a magnetic system. One complete set of the characteristic of kagome lattice includes a Dirac point (DP1) above E_F, a saddle point (SP) near E_F and a flat band (FB1) locates at ~ 0.4 eV below E_F across the whole BZ. They show negligible k_z dispersion, suggesting the major 2D characters of the kagome structure in YMn_6Sn_6. The DFT+DMFT calculations with orbital-resolved electronic structures further confirm the 2D features with the in-plane orbital composition of $d_{xy}/d_{x^2-y^2}$. Moreover, we detected the existence of extra kagome characters, including a Dirac point (DP2) and a flat band (FB2) in the vicinity of E_F. The DP2 has a $d_{xy}/d_{x^2-y^2}$ with mixture of d_{z^2} orbital character, and presents a weak dispersion along k_z, while the FB2 is mainly dominated by d_{xz}/d_{yz} orbitals. In the presence of SOC, the flat band and Dirac point have Chern numbers arising from the non-trivial Berry phase and supporting the orbital magnetism [32]. Altogether, these topological non-trivial bands in the kagome material will help understand the relationship between electronic/magnetic correlation and peculiar lattice geometry, and open an opportunity in manipulating the topological properties in magnetic materials.

Results

The crystal structure and transport property of YMn_6Sn_6. Kagome compound YMn_6Sn_6 has a hexagonal structure with space group $P6/mmm$ (No. 191). It contains three kinds of Sn sites, stacking of Y-Sn3 layer and Mn-Sn1-Sn2-Sn1-Mn slab, with double Mn kagome lattice layers as shown in Fig. 1c. The Sn2 atoms form the honeycomb lattice located at the center of Mn-Sn1-Sn2-Sn1-Mn slab. As for the Mn kagome layers, neutron diffraction experiments reported FM coupling in each kagome bilayer, along with c-axis AFM coupling between the bilayer to the next bilayer below room temperature [33, 34].
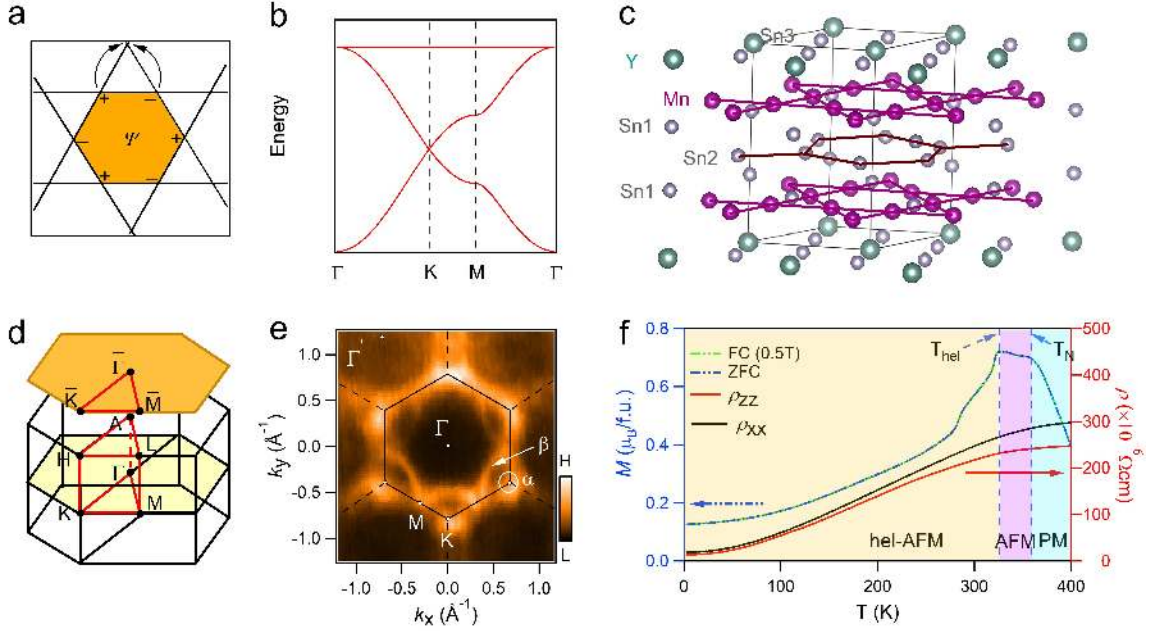
Fig. 1 Crystal and electronic structures of YMn$_6$Sn$_6$. (a) Confinement of electron eigenstate induced by destructive interference in kagome lattice with NN hopping. (b) Tight-binding calculation of band structure of kagome lattice with NN in-plane hopping without SOC, featuring the Dirac cone at the BZ corner K point, a saddle point at BZ boundary M point, and a FB over the whole BZ. (c) Crystal structure of YMn$_6$Sn$_6$ with space group $P6/mmm$ (No. 191). (d) 3D and projected BZs of YMn$_6$Sn$_6$ with marked high-symmetry points. (e) Photoemission intensity plot measured with 138-eV photons at $E_F \pm 10$ meV in the $k_z \sim 0$ plane. Hexagonal BZs are marked with black lines. (f) Magnetization as a function of temperature with zero field-cooling and field-cooling at $B = 0.5$ T along the [100] direction. Temperature dependence of longitudinal resistivity ρ_{xx} and ρ_{zz} with zero-field.

Figure 1d shows the 3D BZ with high-symmetry points and projected BZ along c-axis. In Fig. 1e, the integrated intensity at E_F ± 10 meV obtained from ARPES measurement at $k_z \sim 0$ plane is shown to represent the Fermi surfaces. There exist two pockets centered at $\bar{K}$ point as marked, both with strong matrix element effects. The large one (β) is clearly identified in the 1st BZ but weaker in the 2nd BZ. It looks like an "arc-like" band in the 1st BZ and crosses the zone boundary near M, forming a closed "triangle"-like Fermi pocket. The small one (α) is more clearly visible in the 2nd BZ than in the 1st BZ, and forms a smaller pocket around $\bar{K}$. Figure 1f shows the magnetization as a function of temperature with zero field-cooling and field-cooling at $B = 0.5$ T along the [100] direction. Two transformative peaks at $T_N = 359$ K and $T_{hel} = 326$ K are observed. The former temperature corresponds to the paramagnetism-antiferromagnetism phase transition. The latter corresponds to a transition from an AFM order along the c-axis above T_{hel} to a c-axis helical order with in-plane FM order at low temperature, consistent with the previous results [33–36]. Moreover, the temperature dependence of longitudinal resistivity ρ_{xx} and ρ_{zz} with zero-field shows a metallic behavior with weak anisotropy, similar to GdMn$_6$Sn$_6$ [37].

The complete characteristics of kagome structure. In order to investigate the kagome lattice related topological electronic
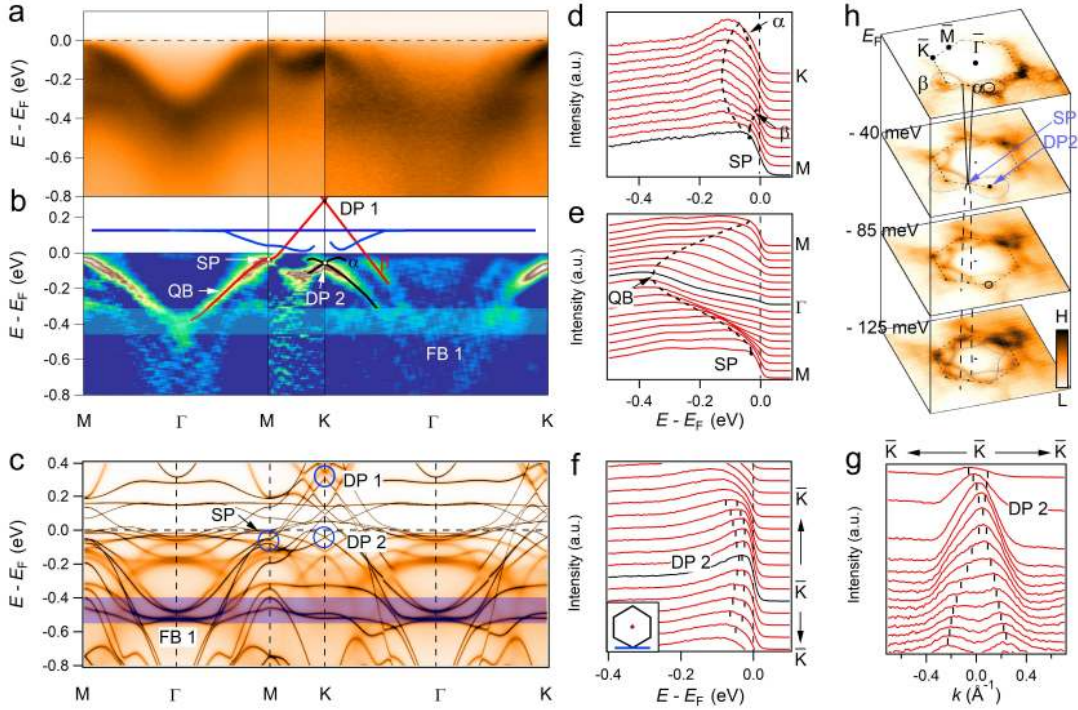
Fig. 2 Band structure evolution in the 1st **BZ.** (a) Photoemission intensity plots of YMn$_6$Sn$_6$ along Γ–M–K–Γ in the $k_z \sim 0$ plane. (b) Corresponding second derivative plots of (a). The blue-colored region highlights the manifestation of the kagome flat band at the binding energy of about 0.4 eV. The appended colored lines serve as guides to the bands, which are extracted from DFT+DMFT calculations. (c) DFT+DMFT calculated ARPES in the FM state with SOC and with the experimentally determined E_F shifted downwards about 76 meV. Dirac point (DP1 and DP2), saddle point (SP) and flat band (FB1) are indicated by the blue circles and blue-colored region, respectively. (d,e) EDC plots along K–M and M–Γ–M, respectively. (f,g) EDC and MDC plots along the $\bar{K}$–$\bar{K}$–$\bar{K}$ direction, with the momentum path indicated as inset. (h) Constant energy maps at different binding energies.

structure, we measured the band structures in the 1st BZ at $k_z \sim 0$ plane along with the high-symmetry lines. The intensity plots along the Γ–M–K–Γ line and the corresponding second derivative plots are shown in Fig. 2a, 2b, respectively. Along Γ–M, one can clearly see a quadratic band (QB) with its bottom at about 0.4 eV below E_F at Γ dispersing upward towards M, and gradually becoming flat at the M point. Along M–K, an electron-like band disperses linearly upward towards E_F and acrosses E_F about one third between M and K, labeled as β in Fig. 1e. At M point, it conforms to the dispersion of SP at $E_B \sim 40$ meV, as marked in Fig. 2b. From intensity plot along Γ–K, the β band passes through the E_F, forming a large holelike FS around K point, which can be more clearly seen in second derivative plots (Fig. 2b). This β band forms a Dirac point (DP1) at about 0.3 eV above E_F, as indicated by the blue circle in Fig. 2c. Another feature is a flat band at about 0.4 eV below E_F, FB1, which exists through the whole BZ. It can be regarded as a direct consequence of quantum phase interference effects in the kagome lattice, as shown in Fig. 1a. This flat band feature has a narrow bandwidth and the intensity is enhanced along Γ–K due to the matrix element effect. The band dispersion closely follows the DFT+DMFT calculations shown in Fig. 2c. In particular, it exhibits the complete characteristics of kagome electronic structure, a flat band (FB1) over the whole BZ touching a quadratic band at Γ point that emerges from the Dirac band (DP1) at K point and forms a saddle point (SP) at M.

At the K point, a linearly dispersing Dirac point (DP2) is also found at around 45 meV below E_F, which is also characteristic of the band structure as a result of kagome lattice as previously observed in FeSn and CoSn [25, 28, 29]. According to our DFT+DMFT calculated orbital-resolved electronic structures in FM configuration, the DP2 arises from the spin-polarized band
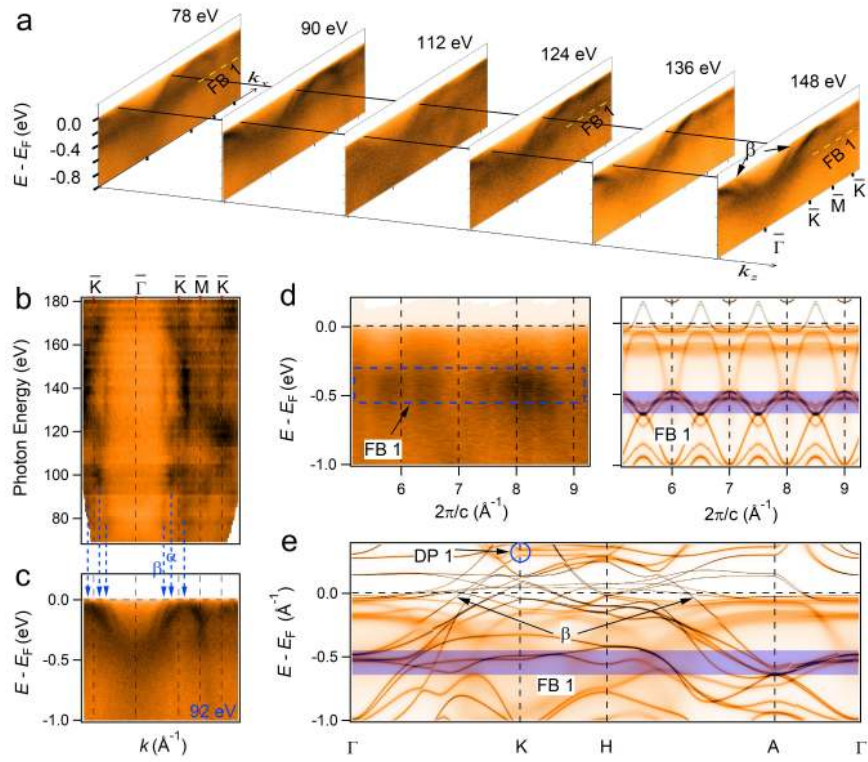
Fig. 3 Photon-energy-dependence measurement of YMn$_6$Sn$_6$. (a) Photoemission intensity plots of YMn$_6$Sn$_6$ with variable photon energies along $\Gamma(A)$–$K(H)$, the flat band (FB1) locates at the binding energy of about 0.4 eV through the whole BZ. The β band appears in every photon energy. (b) ARPES intensity map at E_F in the $k_\parallel$-k_z plane with variable photon energies along $\Gamma(A)$–$K(H)$, showing a well defined 2D-like band structure. (c) Energy-momentum dispersion of YMn$_6$Sn$_6$ measured at $h\nu$ = 92 eV ($k_z \sim 0.6\,\pi/c$). (d) Photoemission intensity plot and DFT+DMFT calculated ARPES in the FM state with SOC along the Γ–A direction, respectively. (e) DFT+DMFT calculated ARPES in the FM state with SOC along Γ–K–H–A–Γ, with the experimentally determined E_F shifted downwards about 76 meV. The blue-colored region highlights the manifestation of the kagome flat band.

with minority-spin state, as shown in the Fig. S5. The DP2 can be also clearly seen from the energy distribution curves (EDCs) and momentum distribution curves (MDCs) in Fig. 2f and Fig. 2g, respectively. With consideration of SOC, a small bandgap <10 meV opens at DP2, adding a mass term to the linearly dispersive band, and a massive Dirac fermion thus can be formed. In consideration of in-plane FM configuration, it could realize a spin-polarized Dirac fermion with a non-trivial Chern gap in YMn$_6$Sn$_6$ as previously observed in TbMn$_6$Sn$_6$ by scanning tunneling microscopy/spectroscopy (STM/S) measurement [18]. In our result, this non-trivial Dirac fermion is in the occupied state and closer to E_F than in TbMn$_6$Sn$_6$, and contributes to the intrinsic anomalous Hall effect in transport measurement [38].

Figure 2h shows a series of constant energy evolution maps in the $k_z \sim 0$. We notice that the β band constitutes a hole pocket and the α band holds an electron pocket around K point. Along with the energy going from E_F to higher binding energy, the hole pockets gradually expand and the branches of β band get closer to each other along K–M–K, finally, touching at SP with the binding energy of ~ 40 meV. Further away from the SP, the band forms a hole band along Γ–M. At M point, the band dispersion conforms a SP at ~ 40 meV below E_F. The α pocket firstly shrinks into a single point and then expands forming a DP at about $E_B = 45 \pm 10$ meV.

In Figs. 3a and 3b, we show the ARPES data along Γ–K–M–K with photon energies from 70 to 180 eV, which covers near four BZs along k_z. In Fig. 3a, one can see that the band dispersions show no qualitative change at various photon energies. Especially, the β band shows no noticeable k_z dependence, which is better identified by the constant crossing point of $k_{F,\parallel}$ in
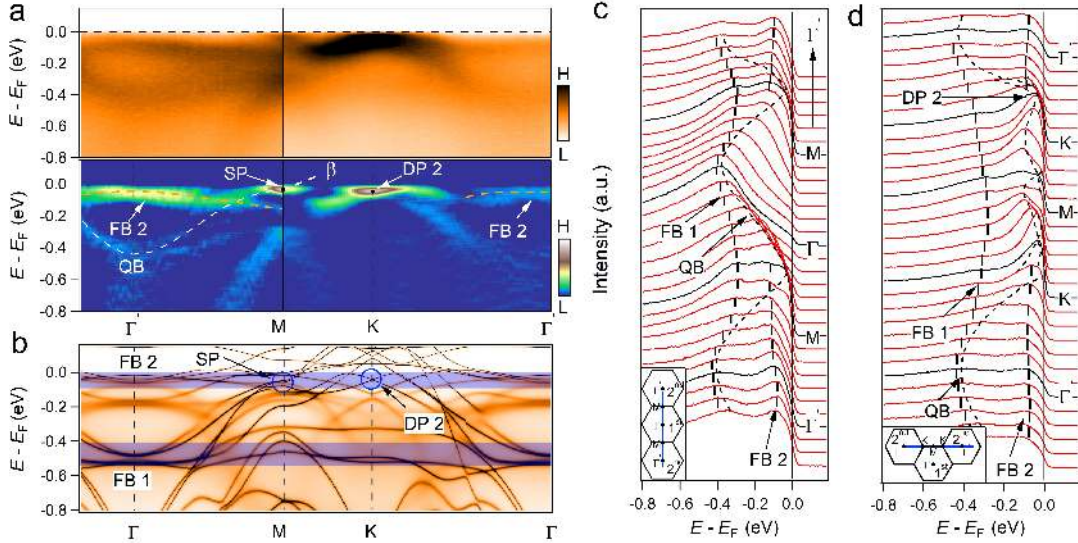
Fig. 4 Band structure evolution in the 2nd BZ. (a) Photoemission intensity plots and corresponding second derivative plots of YMn_6Sn_6 in 2nd BZ along Γ–M–K–Γ in the $k_z \sim 0$ plane. The dashed lines are served as guides to the eyes. (b) DFT+DMFT calculated ARPES in the FM state with SOC to according to the corresponding path of (a) and with experimental E_F. Dirac point (DP2), saddle point (SP) and flat band (FB) are indicated by the blue circles and blue-colored regions, respectively. (c,d) EDC plots along the high-symmetry lines, with the momentum paths indicated as inset. The flat bands (FB1 and FB2) and the parabolic band (QB) are indicated by the black dashed lines with thick and thin, respectively.

Fig. 3b. The FB1 at about 0.4 eV below E_F is also presented in every photon energy, with a limited bandwidth (does not exceed 150 meV) along Γ–A as shown in Fig. 3d, indicating a near 2D character of the band. Figure 3b shows the integrated intensity at $E_F \pm 10$ meV in ΓK–AH plane which covers part of K–M–K at extended in-plane BZs. The β band shows a little variation, further confirms the 2D-like character and ensures the 2D Dirac cone of DP1. The Dirac-related α band around $\bar{K}$ also displays a negligible dispersion along k_z, while one branch has a strong intensity modulation around the Dirac fermion associated with strong matrix element effect, similar to FeSn and CoSn [25, 29]. All the k_z dependence supports the quasi-2D characters of the DP1, DP2 and FB1 bands. An explanation of the 2D-like band structure is that the bands mainly originate from the orbitals confined by the kagome lattice.

To confirm the speculation of the orbital characters in the helical magnetic state along c-axis, we carry out the DFT+DMFT calculations in FM configuration with SOC and show the results in Fig. 3e and Fig. S4. In the DFT+DMFT calculated spectra, we downshift the chemical potential of 76 meV to match the experiment value E_{exp} mostly caused by a chemical doping of the sample. The DFT+DMFT calculated orbital-resolved ARPES in FM configuration without SOC is shown in Fig. S5. The calculations in the FM configurations agreed well with the observation, it shows that the β band mainly originates from the minority-spin branch of $d_{xy}/d_{x^2-y^2}$ orbitals. It forms the DP1 at $\sim$0.3 eV above E_F and shows negligible dispersion along K–H as shown in Fig. 3e. The FB1 passing through the whole in-plane BZ originates from the minority-spin branch of the in-plane $d_{xy}/d_{x^2-y^2}$ orbitals, and has a limited bandwidth at the entire BZ district.

Signature of phase-destructive flat band near E_F. A feature that is faint in the 1st BZ but more clearly visible in the 2nd BZ is

the existence of another flat band near E_F at the BZ center, labeled as FB2 in Fig. 4. In Fig. 4a, the ARPES intensity plots and the corresponding second derivative plots along the Γ–M–K–Γ lines of the 2nd BZ at $k_z \sim 0$ plane are shown. In the 2nd BZ, a spectral weight close to E_F with binding energy $\sim 60 \pm 20$ meV is clearly seen and extends over a large part of the BZ except around the K points due to the intensity leakage from the Dirac bands. In comparison, the intensity of the β and FB1 bands are stronger in the 1st BZ but become feeble in the extended BZ. We assign the contrasting behaviors between FB2 and FB1+β bands to the strong matrix element effect [27, 39] due to the different parity, symmetries or spin-polarization of the bands. In Fig. 4b, we present the DFT+DMFT calculations of the band structure in the FM state with SOC, with a downshift adjustment of the chemical potential of 76 meV as in Fig. 3e. Figure 4c, 4d show EDC plots over more than one BZ along the high-symmetry line as marked in the insets. The contrast of the intensity among different BZs is shown, and the flat bands (FB1 and FB2) and the Dirac point (DP2) can be confirmed unambiguously. For the FB1, it is degenerate with the QB bottom at the center of the BZ (Γ) without SOC. With the consideration of SOC, the two bands further hybridize and open a gap $\sim 40 \pm 10$ meV, which is similar to the results in PM CoSn [28]. The FB2 declines weakly close to M and K points. It is noticed that the peak width becomes broader and the intensity becomes weaker near M and K points, which cause the expected Dirac points feature blurry and nearly indistinguishable and in agreement with the DFT+DMFT calculations in Fig. 4b. In conventional DFT calculations, there should be more band features in magnetic state, and several kagome-related structures are expected. However, in the DFT+DMFT calculations with consideration of correlation effect which is normally present in magnetic system, the broadness and the weaker intensity cause the smearing out of the band, *e.g.* some band features around M, K and along M–K.

We also present the evolution of the FB2 as a function of out-of-plane momentum k_z measured in the in-plane-2nd-BZ along Γ'-A' as shown in Fig. S3. The FB2 displays a weak dispersion over more than one BZ along k_z. Combining its in-plane flat dispersion in the $k_z \sim 0$ plane, weak dispersion along k_z, and the DFT+DMFT calculated orbital-resolved ARPES as shown in Fig. S5, we assign the orbital character of FB2 to d_{xz}/d_{yz} orbitals. It is worth notice that there exists an out-of-plane d_{z^2} orbital with a steep k_z dispersion and crossing E_F at certain k_z, it thus might contribute to the c-axis conductivity in our transport measurements. Further, the FB1 displays a limited bandwidth (<150 meV) along k_z in the 2nd BZ as shown in Fig. S3. It is consistent with results in the 1st BZ with the in-plane $d_{xy}/d_{x^2-y^2}$ orbital composition, as discussed earlier. According to the spin-polarized DFT+DMFT calculations, FB2 with a high density of states (DOS) around the E_F is from the majority-spin state, indicating its singly spin degenerate origin. FB2 is the first momentum-space evidence of the flat band really close to E_F in the magnetic kagome system, which could give interesting phenomena such as orbital magnetism [32].

The band calculations and discussions. To take into account the strong electronic correlation effect of the Mn 3d electrons, in the DFT+DMFT calculations, we include an onsite Coulomb interaction parametrized with a Hubbard $U = 4.0$ eV and a Hund's coupling $J = 0.7$ eV among the Mn 3d electrons in both the PM and FM states. In the PM state, the mass enhancements of the Mn 3d electrons near the E_F are about 5-7, which are similar to the values in some iron chalcogenide superconductors [40]. The fluctuating local moment of Mn 3d electrons, namely, the average value of $g[S(S+1)]^{1/2}$, is about 3.9 μ_B with an effective spin $S =1.5$, indicating YMn$_6$Sn$_6$ has a large fluctuating local moment due to the Hund's rule coupling. Combining with its metallic behavior, we conclude that YMn$_6$Sn$_6$ is a strongly correlated Hund's metal [40].

When the Mn 3d local moments are partially frozen and form long-range static FM order in the hexagonal ab plane, the mass enhancements of the Mn 3d electrons near the E_F are substantially reduced to about 2-3. The fluctuating local moment of Mn 3d electrons remains the same value as in the PM state whereas the statically ordered moment is 2.1 μ_B, which is in excellent agreement with experimental measurement [33, 38].

In the PM state, the YMn$_6$Sn$_6$ has two major characters, including the strong electronic correlation and the kagome related features. The kagome structure has a flat band, while the strong correlation gives extra mass enhancement. These combinations will contribute large DOS around E_F and could cause several instabilities, such as charge density waves [41], superconductivity [12, 42] or magnetic instability [9, 43]. In the magnetic state, the spin degeneracies are lifted, and a few spin-polarized branches shift below E_F. ARPES data reveal the existence of flat band with large DOS and Dirac point near E_F in YMn$_6$Sn$_6$, these bands are thus of singly spin degenerate branches. With consideration of SOC, Chern gaps are opened and Chern numbers are assigned

to each band correspondingly.

These spin-polarized bands carry Berry curvatures and also cause the orbital magnetism. The existence of an orbital magnetic moment has been reported in $Co_3Sn_2S_2$, and was attributed to the kagome flat band [32]. However, the ARPES observation of flat band near E_F has not been reported in $Co_3Sn_2S_2$ yet. The orbital magnetism of the flat band of tight-binding model in kagome lattice with Kane-Mele SOC was calculated in Fig. S7, which is closely related to the Berry curvature. Both the FB with non-zero group velocity part and the massive Dirac fermion will contribute to the orbital magnetism. Our ARPES results first reveal FB and Dirac fermion near E_F with orbital-selective characters, so multi orbital-magnetisms are expected.

In summary, based on ARPES measurement and in combination with theoretical calculations, we have fully revealed the band structure of magnetic kagome YMn_6Sn_6, and presented the first experimental observation of the complete characteristics of kagome lattice near E_F with spin polarization and non-trivial topological properties. The Dirac point and flat band near E_F arise from the spin-polarized band with intrinsic Berry curvature may explain the anomalous Hall effect observed in transport measurements and the orbital magnetic moment observed in STM/S measurement. As an ideal candidate for magnetic kagome lattice material with the electronic structure near E_F, it opens up a new avenue to comprehend the intrinsic properties of magnetic topological electronic material. Furthermore, if the non-trivial band structures–Dirac points, flat band and/or saddle point are further tuned properly, it would possibly realize more versatile quantum phenomena in such material.

Methods

Sample growth and characterizations Single crystals of YMn_6Sn_6 were grown by using Sn flux. Y lumps (purity 99.99 %), Mn granules (purity 99.9 %) and Sn grains (purity 99.99 %) with a molar ratio of Y:Mn:Sn=1:6:30 were put into an alumina crucible and sealed in a quartz ampoule under partial argon atmosphere. The sealed quartz ampoule was heated up to 1273 K and held for 24 hours. Then it was cooled down slowly to 873 K at a rate of 5 K/hours. Finally, the ampoule was taken out from the furnace and decanted with a centrifuge to separate YMn_6Sn_6 crystals from excess Sn flux. Magnetization and electrical transport measurements were carried out by using Quantum Design PPMS-14 T.

ARPES measurements. ARPES measurement were performed at the Dreamline and 03U beamline of the Shanghai Synchrotron Radiation Facility (SSRF), and 1-squared ARPES end-station of BESSY. The optimal energy and angular resolutions were set to 20 meV and 0.2°, respectively. Samples were cleaved *in situ* along (001) surface. During the measurements, the temperature was kept at 25 K and the pressure was maintained less than 5×10^{-11} Torr.

DFT+DMFT calculations. The electronic structures of YMn_6Sn_6 were computed by using DFT+DMFT [44]. The DFT part is based on the full-potential linear augmented plane wave method implemented in WIEN2k [45]. The Perdew-Burke-Ernzerhof generalized gradient approximation [46] is used for the exchange correlation functional. DFT+DMFT was implemented on top of WIEN2k and was described in details in Ref. 47. In the DFT+DMFT calculations, the electronic charge was computed self-consistently on DFT+DMFT density matrix. The quantum impurity problem was solved by the continuous time quantum Monte Carlo method [48, 49] with a Hubbard $U = 4.0$ eV and Hund's rule coupling $J = 0.7$ eV. The experimental crystal structure [50] (space group P6/mmm, No. 191) of YMn_6Sn_6 with lattice constants $a = b = 5.512$ Å and $c = 8.984$ Å was used in the calculations.

calculations used high performance computing clusters at BNU in Zhuhai and the National Supercomputer Center in Guangzhou.

Competing Interests

The authors declare no competing interests.

Correspondence

Correspondence and requests for materials should be addressed to Z.L. (lzh17@mail.sim.ac.cn), Z.Y. (yinzhiping@bnu.edu.cn), H.L. (hlei@ruc.edu.cn) and S.W. (scw@ruc.edu.cn).

[1] Han, T.-h. *et al.* Fractionalized excitations in the spin-liquid state of a kagome-lattice antiferromagnet. *Nature* **492**, 406–410 (2012).

[2] Zhou, Y., Kanoda, K. & Ng, T.-k. Quantum spin liquid states. *Rev. Mod. Phys.* **89**, 025003 (2017).

[3] Thouless, D. J., Kohmoto, M., Nightingale, M. P. & den Nijs, M. Quantized Hall conductance in a two-dimensional periodic potential. *Phys. Rev. Lett.* **49**, 405–408 (1982).

[4] Qi, X.-L., Wu, Y.-S. & Zhang, S.-C. Topological quantization of the spin Hall effect in two-dimensional paramagnetic semiconductors. *Phys. Rev. B* **74**, 085308 (2006).

[5] Xiao, D., Chang, M.-C. & Niu, Q. Berry phase effects on electronic properties. *Rev. Mod. Phys.* **82**, 1959–2007 (2010).

[6] Ohgushi, K., Murakami, S. & Nagaosa, N. Spin anisotropy and quantum Hall effect in the kagomé lattice: Chiral spin state based on a ferromagnet. *Phys. Rev. B* **62**, R6065–R6068 (2000).

[7] Liu, Z., Liu, F. & Wu, Y.-S. Exotic electronic states in the world of flat bands: From theory to material. *Chin. Phys. B* **23**, 077308 (2014).

[8] Mielke, A. Exact ground states for the Hubbard model on the kagome lattice. *J. Phys. A-math. Gen.* **25**, 4335–4345 (1992).

[9] Tasaki, H. Ferromagnetism in the Hubbard models with degenerate single-electron ground states. *Phys. Rev. Lett.* **69**, 1608–1611 (1992).

[10] Mielke, A. Ferromagnetism in the Hubbard model on line graphs and further considerations. *J. Phys. A-math. Gen.* **24**, 3311–3321 (1991).

[11] Peotta, S. & Törmä, P. Superfluidity in topologically nontrivial flat bands. *Nat. Commun.* **6**, 8944 (2015).

[12] Imada, M. & Kohno, M. Superconductivity from flat dispersion designed in doped Mott insulators. *Phys. Rev. Lett.* **84**, 143–146 (2000).

[13] Wu, C., Bergman, D., Balents, L. & Das Sarma, S. Flat Bands and Wigner crystallization in the honeycomb optical lattice. *Phys. Rev. Lett.* **99**, 070401 (2007).

[14] Wu, C. & Das Sarma, S. p_{xy}-orbital counterpart of graphene: cold atoms in the honeycomb optical lattice. *Phys. Rev. B* **77**, 235107 (2008).

[15] Tang, E., Mei, J.-W. & Wen, X.-G. High-temperature fractional quantum Hall states. *Phys. Rev. Lett.* **106**, 236802 (2011).

[16] Neupert, T., Santos, L., Chamon, C. & Mudry, C. Fractional quantum hall states at zero magnetic field. *Phys. Rev. Lett.* **106**, 236804 (2011).

[17] Xu, G., Lian, B. & Zhang, S.-C. Intrinsic quantum anomalous hall effect in the kagome lattice $Cs_2LiMn_3F_{12}$. *Phys. Rev. Lett.* **115**, 186802 (2015).

[18] Yin, J.-X. *et al.* Quantum-limit chern topological magnetism in $TbMn_6Sn_6$. *Nature* **583**, 533–536 (2020).

[19] Wang, Q., Sun, S., Zhang, X., Pang, F. & Lei, H. Anomalous Hall effect in a ferromagnetic Fe_3Sn_2 single crystal with a geometrically frustrated Fe bilayer kagome lattice. *Phys. Rev. B* **94**, 075135 (2016).

[20] Ye, L. *et al.* Massive Dirac fermions in a ferromagnetic kagome metal. *Nature* **555**, 638–642 (2018).

[21] Kim, K. *et al.* Large anomalous Hall current induced by topological nodal lines in a ferromagnetic van der Waals semimetal. *Nat. Mater.* **17**, 794–799 (2018).

[22] Wang, Q. *et al.* Large intrinsic anomalous Hall effect in half-metallic ferromagnet $Co_3Sn_2S_2$ with magnetic Weyl fermions. *Nat. Commun.* **9**, 3681 (2018).

[23] Liu, E. *et al.* Giant anomalous Hall effect in a ferromagnetic kagome-lattice semimetal. *Nat. Phys.* **14**, 1125–1131 (2018).

[24] Kuroda, K. *et al.* Evidence for magnetic Weyl fermions in a correlated metal. *Nat. Mater.* **16**, 1090–1095 (2017).

[25] Kang, M. *et al.* Dirac fermions and flat bands in the ideal kagome metal FeSn. *Nat. Mater.* **19**, 163–169 (2020).

[26] Lin, Z. *et al.* Dirac Fermions in Antiferromagnetic FeSn Kagome Lattices with Combined Space Inversion and Time Reversal Symmetry. *arxiv* (2019). 1906.05755.

[27] Yang, T. Y. *et al.* Evidence of orbit-selective electronic kagome lattice with planar flat-band in correlated paramagnetic YCr_6Ge_6 (2019). 1906.07140.

[28] Liu, Z. *et al.* Orbital-selective Dirac fermions and extremely flat bands in frustrated kagome-lattice metal CoSn. *Nat. Commun.* **11**, 4002 (2020).

[29] Kang, M. *et al.* Topological flat bands in frustrated kagome lattice CoSn. *Nat. Commun.* **11**, 4004 (2020).

[30] Lin, Z. *et al.* Flatbands and emergent ferromagnetic ordering in Fe_3Sn_2 kagome lattices. *Phys. Rev. Lett.* **121**, 096401 (2018).

[31] Zhang, Y. *et al.* Emergence of Kondo lattice behavior in a van der Waals itinerant ferromagnet, Fe_3GeTe_2. *Sci. Adv.* **4**, eaao6791 (2018).

[32] Yin, J.-X. *et al.* Negative flat band magnetism in a spin-orbit-coupled correlated kagome magnet. *Nat. Phys.* **15**, 443–448 (2019).

[33] Zhang, H. *et al.* Topological magnon bands in a room-temperature kagome magnet. *Phys. Rev. B* **101**, 100405 (2020).

[34] Neubauer, K. J. *et al.* In-plane magnetic field induced double fan spin structure with *c*-axis component in metallic kagome antiferromagnet YMn_6Sn_6 (2020). 2007.12154.

[35] Uhlířová, K. *et al.* Magnetic properties and Hall effect of single-crystalline YMn_6Sn_6. *J. Magn. Magn. Mater.* **310**, 1747–1749 (2007).

[36] Matsuo, A. *et al.* Study of the Mn-Mn exchange interactions in single crystals of RMn_6Sn_6 compounds with R = Sc, Y and Lu. *J. Alloys Compd.* **408-412**, 110–113 (2006).

[37] Asaba, T. *et al.* Anomalous Hall effect in the kagome ferrimagnet $GdMn_6Sn_6$. *Phys. Rev. B* **101**, 174415 (2020).

[38] Wang, Q., Yin, Q., Fujitsu, S., Hosono, H. & Lei, H. Near-room-temperature giant topological Hall effect in antiferromagnetic kagome metal YMn_6Sn_6 (2019). 1906.07986.

[39] Wang, X. P. *et al.* Orbital characters determined from Fermi surface intensity patterns using angle-resolved photoemission spectroscopy. *Phys. Rev. B* **85**, 1–15 (2012).

[40] Yin, Z. P., Haule, K. & Kotliar, G. Kinetic frustration and the nature of the magnetic and paramagnetic states in iron pnictides and iron chalcogenides. *Nat. Mater.* **10**, 932 (2011).

[41] Rice, T. & G.K. Scott. New mechanism for a charge-density-wave instability. *Phys. Rev. Lett.* **35**, 120–123 (1975).

[42] Honerkamp, C. & Salmhofer, M. Magnetic and Superconducting Instabilities of the Hubbard Model at the Van Hove Filling. *Physical Review Letters* **87**, 187004 (2001).

[43] Carleschi, E. *et al.* Double metamagnetic transition in $Sr_4Ru_3O_{10}$. *Phys. Rev. B* **90**, 205120 (2014).

[44] Kotliar, G. *et al.* Electronic structure calculations with dynamical mean-field theory. *Rev. Mod. Phys.* **78**, 865 (2006).

[45] Blaha, P., Schwarz, K., Madsen, G., Kvasnicka, D. & Luitz, J. WIEN2K, An Augmented Plane Wave+Local Orbitals Program for Calculating Crystal Properties. *Karlheinz Schwarz, Techn. Universität Wien, Austria* (2001).

[46] Perdew, J. P., Burke, K. & Ernzerhof, M. Generalized gradient approximation made simple. *Phys. Rev. Lett.* **77**, 3865–3868 (1996).

[47] Haule, K., Yee, C.-H. & Kim, K. Dynamical mean-field theory within the full-potential methods: Electronic structure of $CeIrIn_5$, $CeCoIn_5$, and $CeRhIn_5$. *Phys. Rev. B* **81**, 195107 (2010).

[48] Haule, K. Quantum monte carlo impurity solver for cluster dynamical mean-field theory and electronic structure calculations with adjustable cluster base. *Phys. Rev. B* **75**, 155113 (2007).

[49] Werner, P., Comanac, A., de Medici, L., Troyer, M. & Millis, A. J. Continuous-time solver for quantum impurity models. *Phys. Rev. Lett.* **97**, 076405 (2006).

[50] Malaman, B., Venturini, G. & Roques, B. *Mater. Res. Bull.* **23**, 1629–1633 (1988).
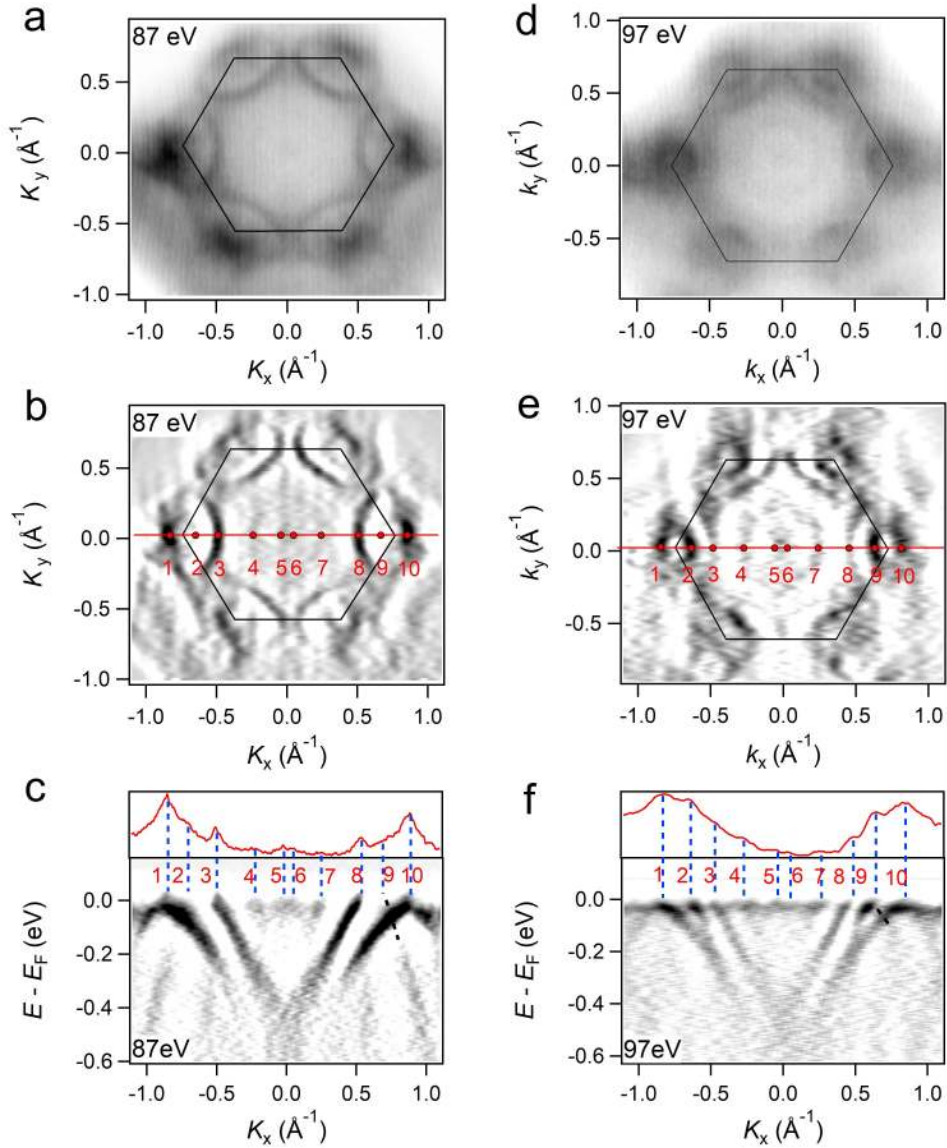
Supplementary Information:

**Spin-polarized Dirac cone, flat band and saddle point in kagome magnet YMn$_6$Sn$_6$**

Li et al.
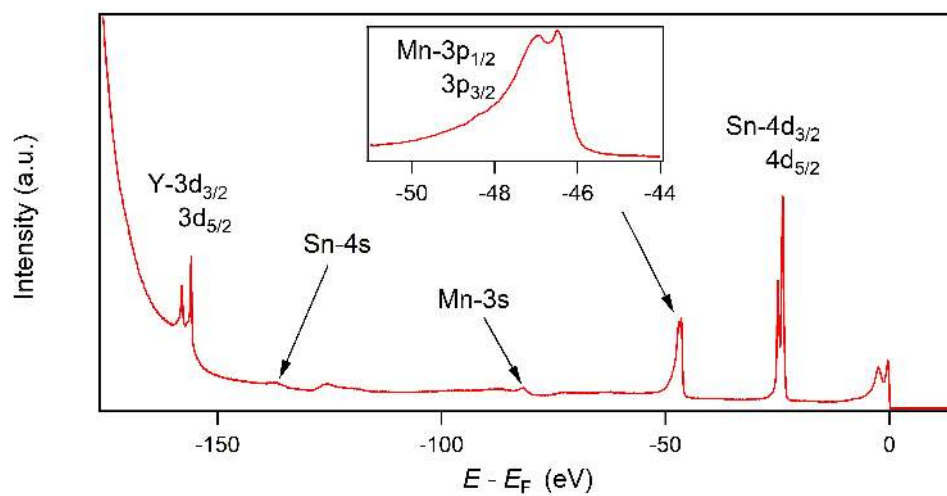
Supplementary Figure 1. **Core-level spectrum of YMn_6Sn_6 taken with** *hv* **= 200 eV. The total angular momentum quantum numbers are labelled for peaks.**

Supplementary Figure 2. (a) Fermi surfaces of YMn_6Sn_6 measured with $h\nu$ = 87 eV. The BZ is marked with the black solid hexagon. (b) The corresponding second derivative plot of a. (c) Energy-momentum dispersions of YMn_6Sn_6 along the high-symmetry direction, marked as the solid red line in b. Momentum distribution curve at Fermi energy is overlaid, with a dashed blue line indicating peaks at k_F. (d-f) Same as (a-c), but taken with 97-eV photons.
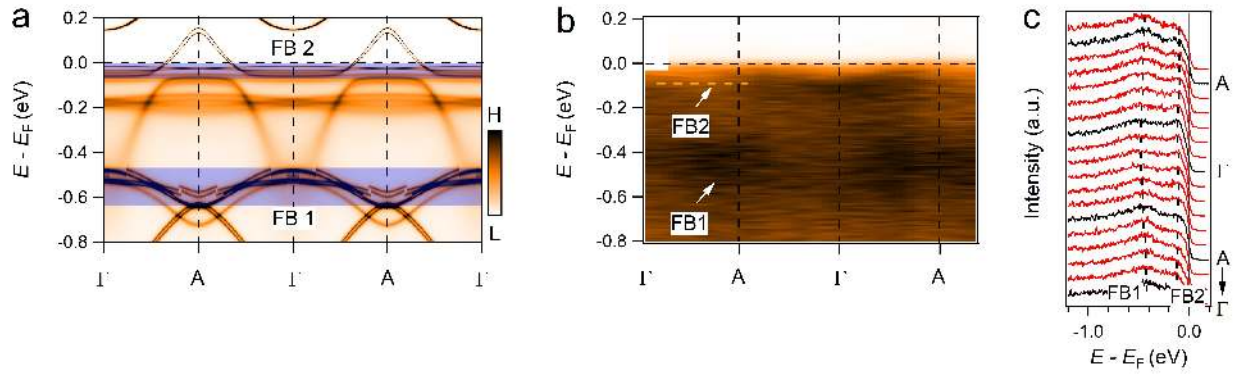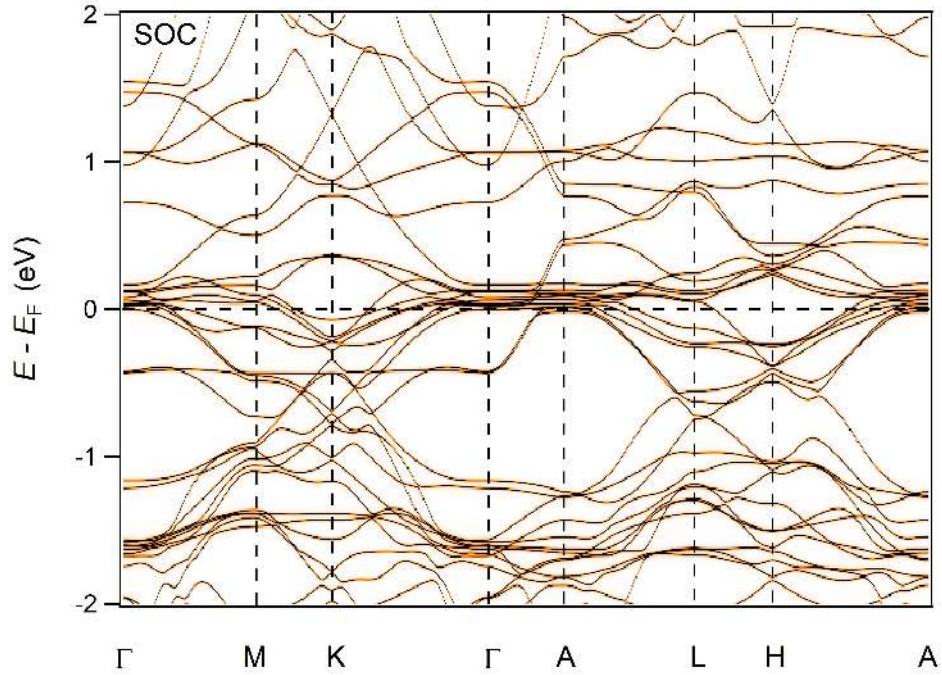
Supplementary Figure 3. **(a) The DFT+DMFT calculation in the FM state with SOC along k_z. Flat bands, FB1 and FB2, are indicated by the color-shaded regions. (b) Intensity plot along the Γ–A direction in the in-plane-2nd BZ. The two flat bands are indicated by the white arrows. The dashed lines are served as guides for eyes. (c) EDCs plot of (b). The FB1 and FB2 are indicated by the black dashed lines.**
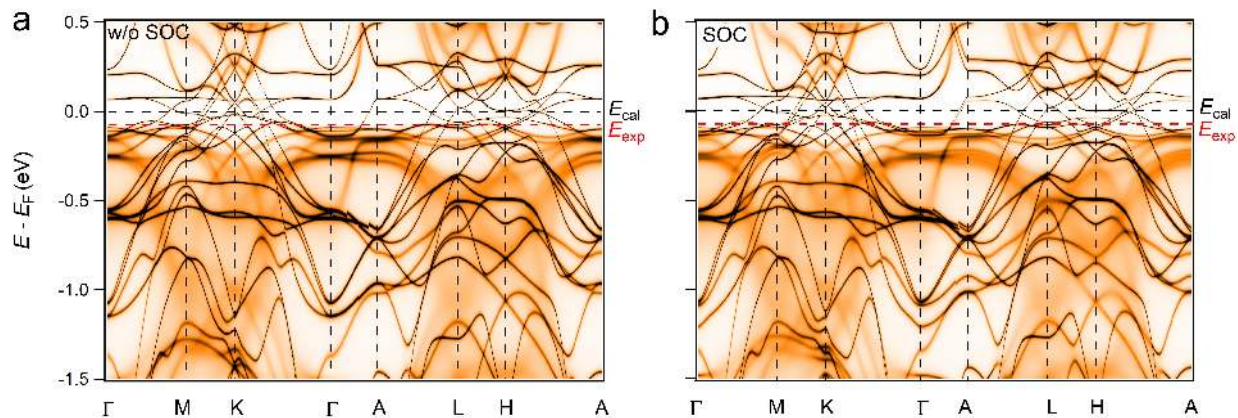
Supplementary Figure 4. The DFT+DMFT calculation of YMn_6Sn_6 in the FM state and (a) without SOC and (b) with SOC along the high-symmetry directions. The dashed red line indicates the experimental Fermi level.
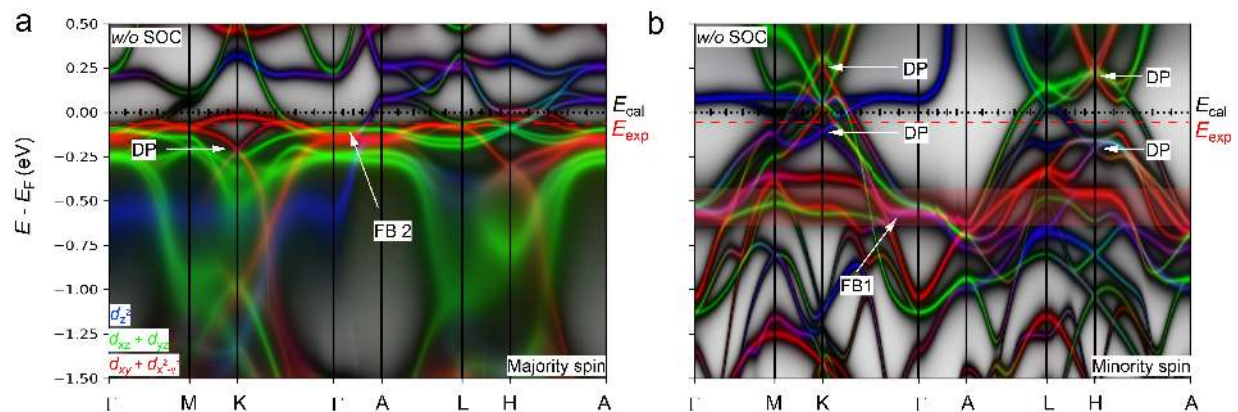
Supplementary Figure 5. The DFT+DMFT calculation with (a) spin-majority and (b) spin-minority states along the high-symmetry directions without SOC and with 3d orbitals projections. The red, green and blue lines indicate the orbitals components of $d_{xy}/d_{x^2-y^2}$, d_{xz}/d_{yz} and d_{z^2}, respectively. The magenta, cyan and light yellow are color mixings of red, green and blue, respectively.

Supplementary Figure 6. The DFT calculation of YMn_6Sn_6 in the nonmagnetic phase with SOC along the high-symmetry directions.
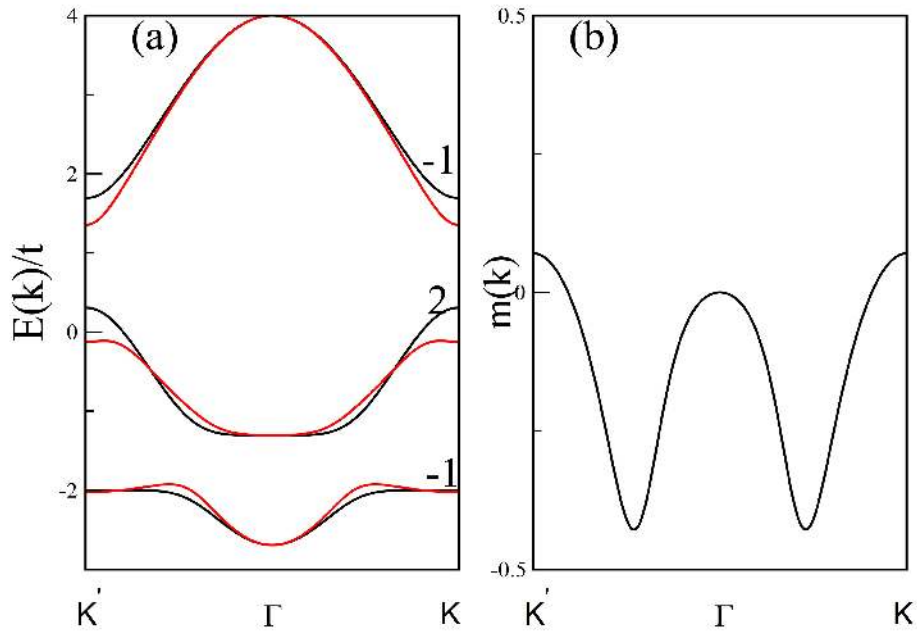
Supplementary Figure 7. (a)Band dispersion along $K' - \Gamma - K$ with $\lambda = 0.2t$. Chern numbers of each band are also shown. Red lines are bands coupling to $m(k)$. (b) $m(k)$ (unit of $\frac{e}{2\hbar}$) of the flat band in (a).

Supplementary Note 1. Sample growth and characterizations. Single crystals of YMn_6Sn_6 were grown by using Sn flux. Y lumps (purity 99.99 %), Mn granules (purity 99.9 %) and Sn grains (purity 99.99 %) with a molar ratio of Y : Mn : Sn = 1 : 6 : 30 put into an alumina crucible and sealed in a quartz ampoule under partial argon atmosphere. The sealed quartz ampoule was heated up to 1273 K and held for 24 hours. Then it was cooled down slowly to 873 K at a rate of 5 K/hour. Finally, the ampoule was taken out from the furnace and decanted with a centrifuge to separate YMn_6Sn_6 crystals from excess Sn flux. Magnetization and electrical transport measurements were carried out by using Quantum Design PPMS-14 T.

Supplementary Note 2. Angle-resolved photoemission spectroscopy experiments. ARPES measurement were performed at the Dreamline and 03U beamline of the Shanghai Synchrotron Radiation Facility (SSRF), and 1-squared ARPES end-station of BESSY. The combined energy resolutions were set to around 20 meV at low photon energies and 28 meV at high photon energies. The angular resolution is 0.2°. Samples were cleaved *in situ*, yielding a flat mirrorlike (001) surface. During the measurements, the temperature was kept at 25 K and the pressure was maintained less than 5×10^{-11} Torr.

We conducted core-level spectroscopy with the photon energy of 200 eV. In supplementary Fig. 1, we present the core-level photoemission intensity plot of YMn_6Sn_6 where the characteristic peaks of Y-3d, Sn-4s/4d, and Mn-3s/3p orbitals are clearly observed, with no extra peaks observed, suggesting the high quality of the crystal and the bulk origin with no surface contribution.

We measured the intensity plots and corresponding second derivative plots of YMn_6Sn_6 with 87-eV and 97-eV photons, as shown in supplementary Fig. 2. The high symmetry cuts with ten crossing points are observed between K–Γ–K line, as indicated with blue dotted lines along the solid red line of supplementary Fig. 2b,e. The Dirac cones locate on the marked between the "1" and "2" or "9" and "10". One branch of the Dirac-like bands could be observed and another one is faint due to the matrix element effect associated with the chirality of the Dirac fermions similar to CoSn and FeSn [1, 2].

Supplementary Figure 3 shows the intensity plots along Γ-A in the 2nd Brillouin zone (BZ). The FB2 is missed in the first BZ due to the matrix element effect, but clearly presented in the second BZ. The FB1 locates at ~ 0.4 eV below E_F with a narrow bandwidth (< 150 meV). The FB2 locates at ~ 0.06 eV below E_F showing nealy no dispersion along k_z.

Supplementary Note 3. Calculations. The electronic structures of YMn_6Sn_6 were computed by using density functional theory combined with dynamical mean field theory (DFT+DMFT) [3]. The density functional theory part is based on the full-potential linear augmented plane wave method implemented in Wien2K [4]. The Perdew-Burke-Ernzerhof generalized gradient approximation [5] is used for the exchange correlation functional. DFT+DMFT was implemented on top of Wien2K and was described in details in Ref. 6. In the DFT+DMFT calculations, the electronic charge was computed self-consistently

on DFT+DMFT density matrix. The quantum impurity problem was solved by the continuous time quantum Monte Carlo (CTQMC) method [7, 8] with a Hubbard U=4.0 eV and Hund's rule coupling J=0.7 eV. The experimental crystal structure [9] (space group P6/mmm, No. 191) of YMn_6Sn_6 with lattice constants a=b=5.512 Å and c=8.984 Å was used in the calculations.

Supplementary Note 4. Orbital magnetism. The orbital magnetism of a wave packet is related to its angular momentum [10, 11],

$$\mathbf{m_n(k)} = -i\frac{e}{2\hbar}\langle \nabla_\mathbf{k} u_n| \times [H(\mathbf{k}) - \epsilon_n(\mathbf{k})]|\nabla_\mathbf{k} u_n\rangle \tag{1}$$

$$= -i\frac{e}{2\hbar}(\langle \frac{\partial u_n}{\partial k_x}|H(\mathbf{k}) - \epsilon_n(\mathbf{k})|\frac{\partial u_n}{\partial k_y}\rangle - c.c.)\mathbf{e_z} \tag{2}$$

$$= -i\frac{e}{2\hbar}\sum_{m\neq n}[\frac{\langle u_n|\frac{\partial H(\mathbf{k})}{\partial k_x}|u_m\rangle\langle u_m|\frac{\partial H(\mathbf{k})}{\partial k_y}|u_n\rangle}{\epsilon_m(\mathbf{k}) - \epsilon_n(\mathbf{k})} - c.c.]\mathbf{e_z} \tag{3}$$

where n, m are band indices. The derivation of Eq.3 can be found in Ref [12], which is similar to the equations of Berry curvature $\Omega_n(\mathbf{k})$ [12, 13].

$$\Omega_n(\mathbf{k}) = i\langle \nabla_\mathbf{k} u_n| \times |\nabla_\mathbf{k} u_n\rangle \tag{4}$$

$$= i(\langle \frac{\partial u_n}{\partial k_x}|\frac{\partial u_n}{\partial k_y}\rangle - \langle \frac{\partial u_n}{\partial k_y}|\frac{\partial u_n}{\partial k_x}\rangle) \tag{5}$$

$$= i\sum_{m\neq n}[\frac{\langle u_n|\frac{\partial H(\mathbf{k})}{\partial k_x}|u_m\rangle\langle u_m|\frac{\partial H(\mathbf{k})}{\partial k_y}|u_n\rangle}{(\epsilon_m(\mathbf{k}) - \epsilon_n(\mathbf{k}))^2} - c.c.] \tag{6}$$

The only change of $\Omega_n(\mathbf{k})$ and $\mathbf{m_n(k)}$ is the extra factor of $H(\mathbf{k}) - \epsilon_n(\mathbf{k})$ in the numerator cancels a $\epsilon_m(\mathbf{k}) - \epsilon_n(\mathbf{k})$ in the denominator.

Supplementary Note 5. Kagome lattice with Kane-Mele SOC and Ferromagnetism. We consider a unit cell of the kagome lattice spaned by the primitive lattice $2\mathbf{a_1} = (2, 0)$, $2\mathbf{a_2} = (1, \sqrt{3})$ and define $\mathbf{a_3} = \mathbf{a_2} - \mathbf{a_1}$. In the ferromagnetic kagome lattice with SOC strength λ, the spinless Hamiltonian in k-space is

$$H(k) = 2t\begin{bmatrix} 0 & \cos\mathbf{k}\cdot\mathbf{a_1} & \cos\mathbf{k}\cdot\mathbf{a_2} \\ \cos\mathbf{k}\cdot\mathbf{a_1} & 0 & \cos\mathbf{k}\cdot\mathbf{a_3} \\ \cos\mathbf{k}\cdot\mathbf{a_2} & \cos\mathbf{k}\cdot\mathbf{a_3} & 0 \end{bmatrix} + 2\lambda i\begin{bmatrix} 0 & \cos\mathbf{k}\cdot(\mathbf{a_2}+\mathbf{a_3}) & -\cos\mathbf{k}\cdot(\mathbf{a_3}-\mathbf{a_1}) \\ -\cos\mathbf{k}\cdot(\mathbf{a_2}+\mathbf{a_3}) & 0 & \cos\mathbf{k}\cdot(\mathbf{a_1}+\mathbf{a_2}) \\ \cos\mathbf{k}\cdot(\mathbf{a_3}-\mathbf{a_1}) & -\cos\mathbf{k}\cdot(\mathbf{a_1}+\mathbf{a_2}) & 0 \end{bmatrix} \tag{7}$$

We choose $\lambda = 0.2t$. The dispersion along $K' - \Gamma - K$ is shown in supplementary Fig. 7(a). Orbital magnetism $\mathbf{m_n(k)}$ of the flat band is shown in supplementary Fig. 7(b).

Supplementary references

---

[1] Kang, M. *et al.* Dirac fermions and flat bands in the ideal kagome metal FeSn. *Nat. Mater.* **19**, 163–169 (2020).

[2] Kang, M. *et al.* Topological flat bands in frustrated kagome lattice CoSn. *Nat. Commun.* **11**, 4004 (2020).

[3] Kotliar, G. *et al.* Electronic structure calculations with dynamical mean-field theory. *Rev. Mod. Phys.* **78**, 865 (2006).

[4] Blaha, P., Schwarz, K., Madsen, G., Kvasnicka, D. & Luitz, J. WIEN2K, An Augmented Plane Wave+Local Orbitals Program for Calculating Crystal Properties. *Karlheinz Schwarz, Techn. Universität Wien, Austria* (2001).

[5] Perdew, J. P., Burke, K. & Ernzerhof, M. Generalized gradient approximation made simple. *Phys. Rev. Lett.* **77**, 3865–3868 (1996).

[6] Haule, K., Yee, C.-H. & Kim, K. Dynamical mean-field theory within the full-potential methods: Electronic structure of CeIrIn$_5$, CeCoIn$_5$, and CeRhIn$_5$. *Phys. Rev. B* **81**, 195107 (2010).

[7] Haule, K. Quantum monte carlo impurity solver for cluster dynamical mean-field theory and electronic structure calculations with adjustable cluster base. *Phys. Rev. B* **75**, 155113 (2007).

[8] Werner, P., Comanac, A., de Medici, L., Troyer, M. & Millis, A. J. Continuous-time solver for quantum impurity models. *Phys. Rev. Lett.* **97**, 076405 (2006).

[9] Malaman, B., Venturini, G. & Roques, B. *Mater. Res. Bull.* **23**, 1629–1633 (1988).

[10] D. Xiao, Q. N., M. C. Chang. *Rev. Mod. Phys.* **82**, 1959 (2010).

[11] D. Xiao, W. Y. & Niu, Q. *Phys. Rev. Lett.* **99**, 236809 (2007).

[12] Chang, M. C. & Niu, Q. *Phys. Rev. B* **53**, 7010 (1996).

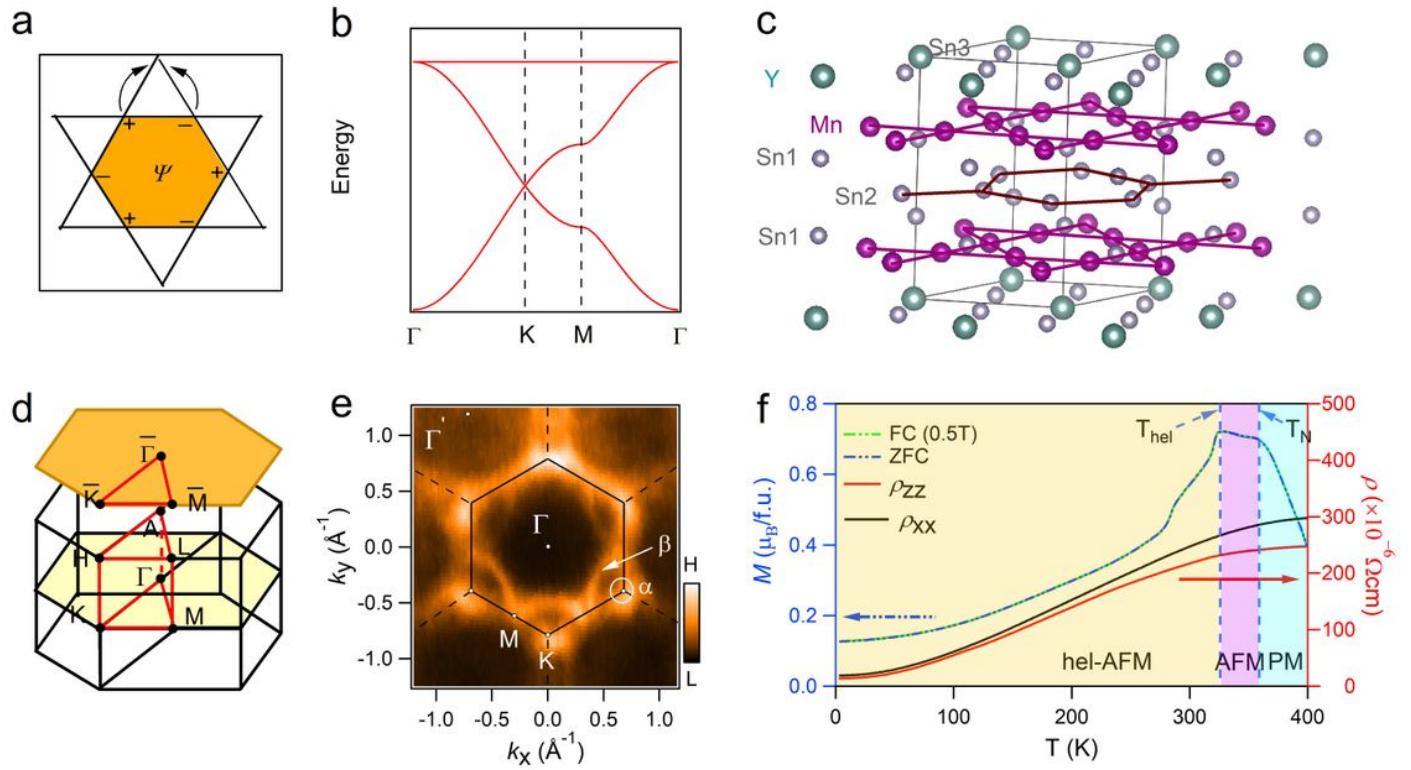[13] T. Thonhauser, I. J. *Mod. Phys. B* **25**, 1429 (2011).

Figures

Figure 1

Crystal and electronic structures of YMn6Sn6. (a) Confinement of electron eigenstate induced by destructive interference in kagome lattice with NN hopping. (b) Tight-binding calculation of band structure of kagome lattice with NN in-plane hopping without SOC, featuring the Dirac cone at the BZ corner K point, a saddle point at BZ boundary M point, and a FB over the whole BZ. (c) Crystal structure of YMn6Sn6 with space group P6=mmm (No. 191). (d) 3D and projected BZs of YMn6Sn6 with marked high-symmetry points. (e) Photoemission intensity plot measured with 138-eV photons at EF ±10 meV in the kz ~ 0 plane. Hexagonal BZs are marked with black lines. (f) Magnetization as a function of temperature with zero field-cooling and field-cooling at B = 0.5 T along the [100] direction. Temperature dependence of longitudinal resistivity pxx and pzz with zero-field.
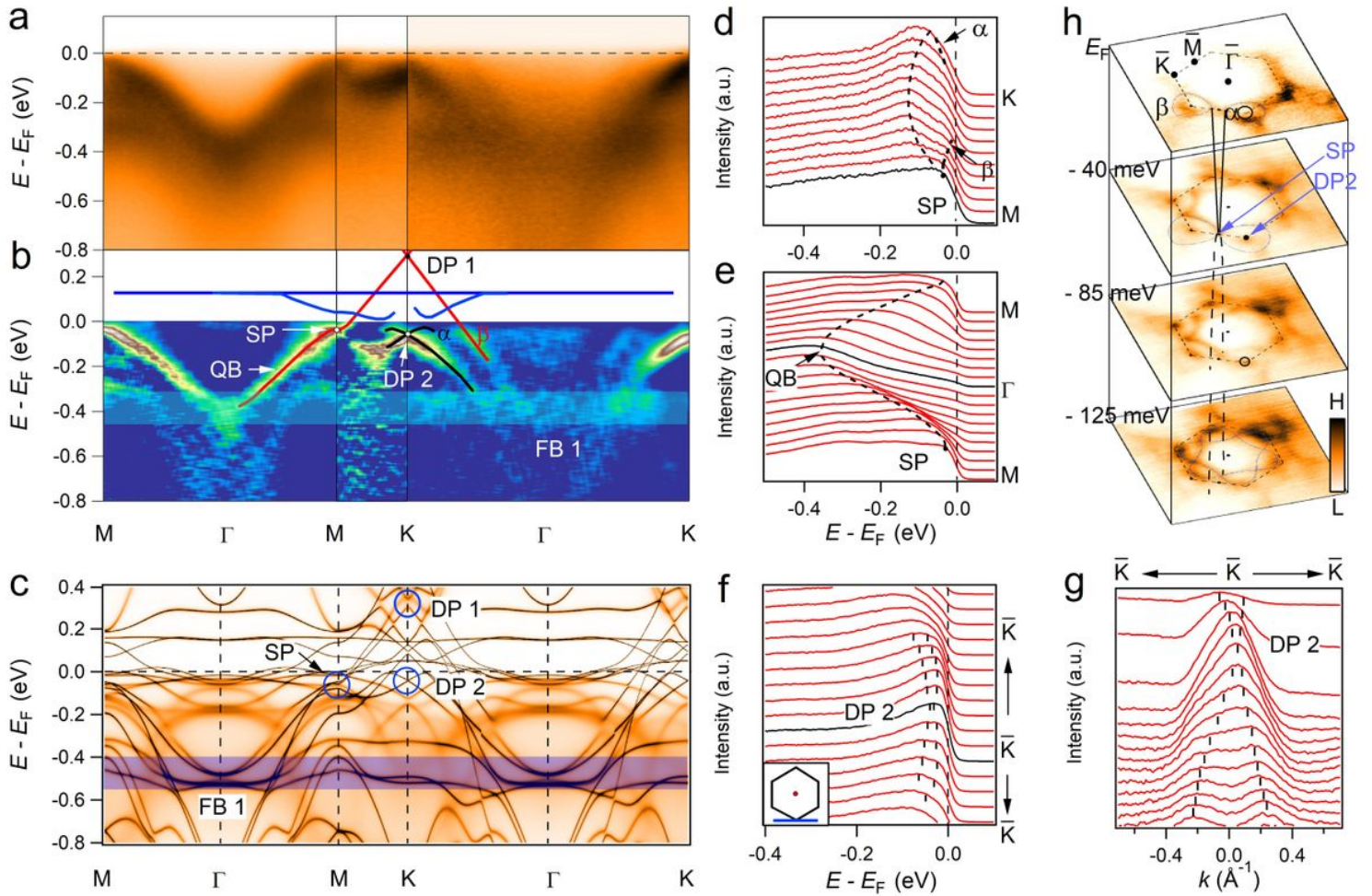
Figure 2

Band structure evolution in the 1st BZ. (a) Photoemission intensity plots of YMn6Sn6 along Γ−M−K−Γ in the kz ⎯ 0 plane. (b) Corresponding second derivative plots of (a). The blue-colored region highlights the manifestation of the kagome flat band at the binding energy of about 0.4 eV. The appended colored lines serve as guides to the bands, which are extracted from DFT+DMFT calculations. (c) DFT+DMFT calculated ARPES in the FM state with SOC and with the experimentally determined EF shifted downwards about 76 meV. Dirac point (DP1 and DP2), saddle point (SP) and flat band (FB1) are indicated by the blue circles and blue-colored region, respectively. (d,e) EDC plots along K−M and M−Γ−M, respectively. (f,g) EDC and MDC plots along the K̄ −K̄ −K̄ direction, with the momentum path indicated as inset. (h) Constant energy maps at different binding energies.
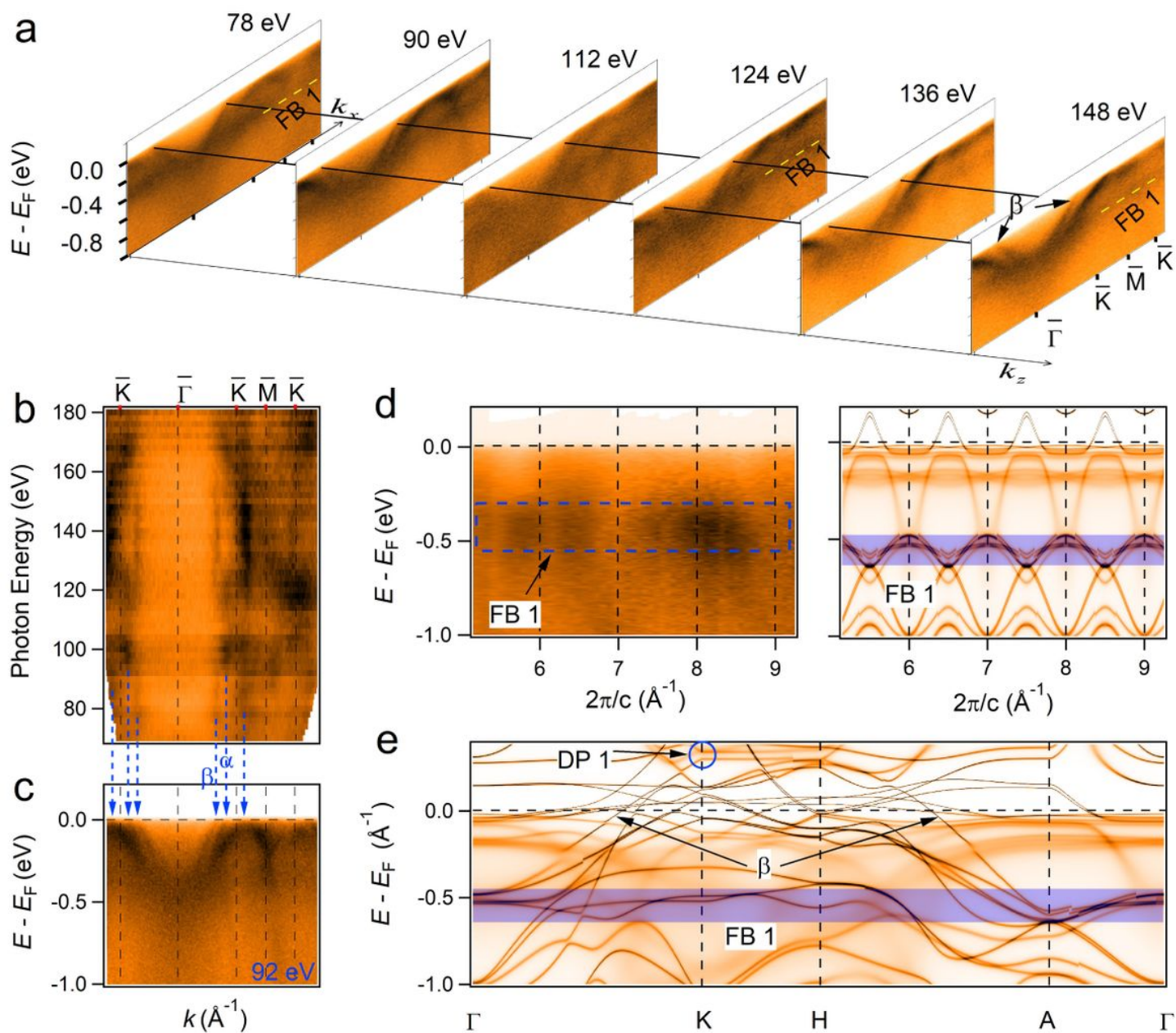
Figure 3

Photon-energy-dependence measurement of YMn6Sn6. (a) Photoemission intensity plots of YMn6Sn6 with variable photon energies along Γ(A)−K(H), the flat band (FB1) locates at the binding energy of about 0.4 eV through the whole BZ. The β band appears in every photon energy. (b) ARPES intensity map at EF in the k⌷-kz plane with variable photon energies along Γ(A)−K(H), showing a well defined 2D-like band structure. (c) Energy-momentum dispersion of YMn6Sn6 measured at hv = 92 eV (kz ⌷ 0.6 π/c). (d) Photoemission intensity plot and DFT+DMFT calculated ARPES in the FM state with SOC along the Γ−A di-rection, respectively. (e) DFT+DMFT calculated ARPES in the FM state with SOC along Γ−K−H−A−Γ, with the experimentally determined EF shifted downwards about 76 meV. The blue-colored region highlights the manifestation of the kagome flat band.
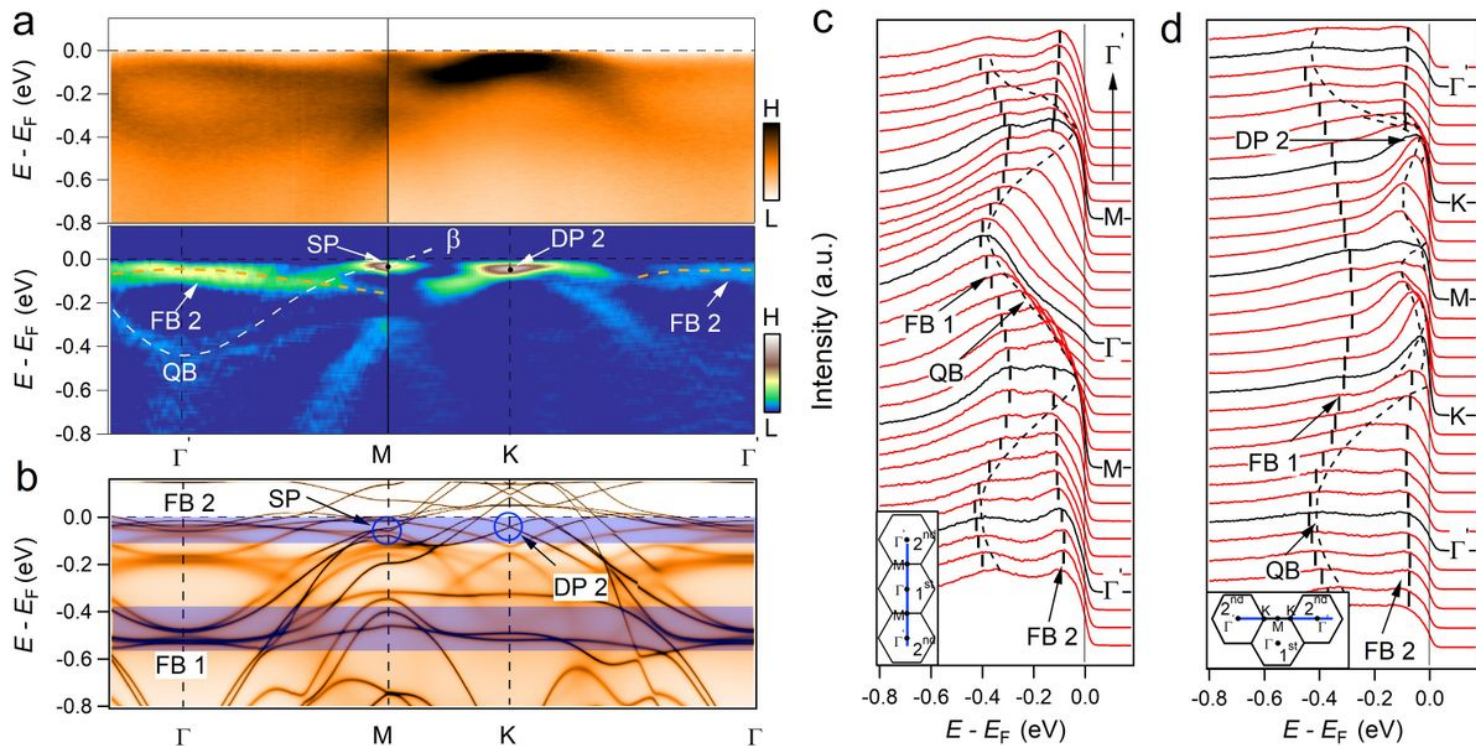
Figure 4

Band structure evolution in the 2nd BZ. (a) Photoemission intensity plots and corresponding second derivative plots of YMn6Sn6 in 2nd BZ along Γ−M−K−Γ in the kz ⎵ 0 plane. The dashed lines are served as guides to the eyes. (b) DFT+DMFT calculated ARPES in the FM state with SOC to according to the corresponding path of (a) and with experi-mental EF. Dirac point (DP2), saddle point (SP) and flat band (FB) are indicated by the blue circles and blue-colored re-gions, respectively. (c,d) EDC plots along the high-symmetry lines, with the momentum paths indicated as inset. The flat bands (FB1 and FB2) and the parabolic band (QB) are indicated by the black dashed lines with thick and thin, respectively.